

# INTEGRATING PASSIVE AND ACTIVE REMOTE SENSING DATA WITH SPATIAL FILTERS FOR URBAN GROWTH ANALYSIS IN URMIA, IRAN

Vahid Isazade<sup>1</sup> , Esmail Isazade<sup>2</sup>, Abdul Baser Qasimi<sup>\*3</sup> , and Ahmed Serwa<sup>4</sup> 

<sup>1</sup> Department of department of geographical science, Kharazmi University, Tehran, Iran

<sup>2</sup> Department of Urban planning, Tarbiat Modares University, Tehran, Iran

<sup>3</sup> Department of geography, Faculty of Education, Samangan university, Samangan, Afghanistan

<sup>4</sup> Faculty of Engineering in El-Mataria, Helwan University, Cairo, Egypt

\* **Correspondence to:** Abdul Baser Qasimi, qasimi.abdul.a@gmail.com.

**Abstract:** Active remote sensing and related technologies are one of the new tools recently used to monitor complications and urban growth. This research aims to investigate the effect of spatial filters on urban complications. The aim of this paper is to compare Lee, Frost and Average spatial filters with Landsat 8 satellite images and radar images with HH/HV polarization to investigate and identify urban features in the west of Urmia City. The results showed that Filterelli with the kernel  $3 \times 3$  had reduced the spike noise in Alus Palsard satellite radar images in identifying the growth of urban tolls. Also, the results of K-means classification, the Lee filter with kernel size  $3 \times 3$  more accurately identifies the urban features of the west of Urmia City. The kappa coefficient was 0.96%, and the overall accuracy of this filter was 97.36%. Therefore, Lee's spatial filter has successfully identified the urban features of west Urmia with high accuracy. This system can be implemented in any other field due to its generality and reliability. This system may be a step towards remote sensing automation.

**Keywords:** Urban growth, Active remote sensing, Passive remote sensing, Lee filter, Urmia.

**Citation:** Isazade, V., E. Isazade, A. B. Qasimi, and A. Serwa (2023), Integrating Passive and Active Remote Sensing Data with Spatial Filters for Urban Growth Analysis in Urmia, Iran, *Russian Journal of Earth Sciences*, 23, ES5012, EDN: TSPARR, <https://doi.org/10.2205/2023es000861>

## 1. Introduction

Fusing different remote sensing data types (active and passive) can improve the performance of any spatial system [Serwa and Saleh, 2021]. The world is developing fast the motion Toward urbanization is built mainly through updating the texture maps [Seto et al., 2012; Sun et al., 2007]. Land use/cover maps are suitable for planning, environmental administration, disaster management, and public education on global development status [Qasimi et al., 2022]. The impacts of the growth of urbanization on the environment consist of triggering possibly destructive feedback such as a massive change in climate, water pollution, and destruction of nature by developing settlement areas [Ghanbari et al., 2022; Mohan and Kandya, 2015; Zia et al., 2015]. Urbanization accelerates significantly, and the number of sizable metropolises continues to grow [Hu et al., 2016]. For multiple years remote sensing of the satellite has been used for continuous mapping and observing various earth countenance consisting of urban objects [Isazade et al., 2022; Yang et al., 2016]. Methods and techniques are desired over manual view methods because of additional effectiveness and accuracy, like time and spatial coverage [Isazade et al., 2022; NISAR, 2018; Podest, 2018]. Some international spaces agencies, including India and the European place agency the National Aeronautics and place command [Attarchi et al., 2020; Podest, 2018], have successfully developed and designed several optical satellites to observe and measure the features of the earth's surface, such as Landsat and IRS series [Kraus, 2003; Li et al., 2020; NISAR, 2018], Sentinel 2 along with artificial crevice radar (SAR) satellites so as RISAT-1, Sentinel 1-6, MODIS Aqua, Terra. In the last few years, optical remote sensing observations are getting outmoded, as expected by their ineffectiveness in piercing past the dense cloudy cover [Kraus, 2003; Li et al., 2020].

## RESEARCH ARTICLE

Received: 15 May 2023

Accepted: 7 July 2023

Published: 30 December 2023



**Copyright:** © 2023. The Authors. This article is an open access article distributed under the terms and conditions of the Creative Commons Attribution (CC BY) license (<https://creativecommons.org/licenses/by/4.0/>).

Nowadays, optical satellites are generally utilized for some schematization and monitoring operations. Though in some positions, it is essential for remote sensing to survey and observe the status of the earth's surface condition in the period of cloud cover and terrible climate conditions [Isazade et al., 2021]. Multispectral satellite images are more general than optical ones due to the variety of spectral resolutions and bands [Serwa and Elbialy, 2021]. Using active sensing data perfectly performs to obtain spatial data [Serwa and Saleh, 2021]. Monitoring surface situations using radar equipment has a different view and provides several states for feature recognition [Alves et al., 2020; Leiva-Murillo et al., 2013]. However, acquiring any radar images comes up with multi-dimensional issues containing quality of the information, cost of acquisition, preprocessing of the data or methods of correction, and enhanced distortion. This data collection becomes offender the efficacy cited by some caused mistakes that need information processing [Betbeder et al., 2015]. A prominent section of the processing functions underscores the drop of extended contortion or noise from the accepted SAR images. In this issue, the European charge holds attended to institute the Program of Copernicus, which designed a novel model mutation toward the accessibility and availability of information to hand over different earth-seeing services by the support of satellites and in site information down six present Copernicus services [Kaushik and Kumar, 2020]. Lines and edges are commonly easy visages to be isolated from a satellite image so that they can be operated for subsequent studies in the domains of image processing, computer perspective, remote sensing, and photogrammetry [Rasche, 2018; Seo, 2018, 2019a,b]. Zakeri et al. [2017] utilized S1 and ALOS-2 PALSAR-2 images for land cover classification in Tehran. Utilizing the backscattering worth on S1 images for the support vector machine classification of land cover by five categories, Kappa stood at 0.30 and the OA 45.70%. Additionally, elements that had surfaces were selected through the PCA and plugged with the backscattering polarized satellite imagery.

Osgouei et al. [2019] used enhanced image classification to map the land cover for Istanbul, acquired from sentinel 2A data, employing SVM. The normalized deference tillage index was utilized to determine built-up elements as the domain of a three-band synthesized image, comprising the vermilion-edging-based normalized dissimilarity vegetation index and the corrected, normalized distinction water index. Camargo et al. [2019] and Lapini et al. [2020] employed SAR imagery for Brazil's equatorial savannah land cover classes and the Mediterranean region's forest classes.

Previous studies also offered MLP, RBF and Support vector machine (SVM) as the exact arranger. Also, the decision tree exhibited a refined version for observing specific land cover categories (e.g., vegetation). Deep learning classifiers are proven perfect [Serwa, 2020]. Li et al. [2020], Mun et al. [2019], and Routray et al. [2020] focused instead on filtering out the performance and worth keeping of an image. Speckle noise can bring down the modality of the image. Due to this reasoning, the assessment has carried a position among untroubled and filtered imagery. The spot degradation is accomplished at the damage by protection data.

Established at this, an equivalent extent has been given to estimating the speckle filtering and filtering efficiency and retinue in detail. Wei and Blaschke [2018] created a collation between supervised classification, object-based, and pixel-based unsupervised category, and the object-based process is recommended for the category of increased-resolution images. Abdollahi et al. [2017] illustrated the road extraction, acquired by SVM, level set method and Otsu's algorithm with Comprehensiveness and feasible Correctness. However, it is limited to images with only a spatial resolution of 0.21 m. Dai et al. [2020] defined path exploitation acquired utilizing Preprocessing, smoothing, segmentation, and eventually and eventually flexible path factor acquiring per a specific histogram MLSOH is intended to extract the road and its orientation by Correctness of 99.54%, with a Totality 97.73%. However, it is not reasonable for the extensive shadow area, and the image is regularly essential to be enhanced. Shi et al. [2019] extracted constructions using artefact features well-found in building measures, figures, tissue, paint, shade, and roof textile. In common, the broadly utilized methodology for remote sensing feature detection is

classification-based. Building extraction is done by separating its elements and applying classification techniques like Support vector machine or RF.

*Isazade et al.* [2021], spectral indices and constructed and non-constructed urban features and their comparison with surface temperature using Landsat satellite images for the city of Tehran were evaluated. Their results showed that VbSWIR\_BI and IBI indices have the highest accuracy compared to other indices. With the increase in construction, the temperature has risen in the central and northern parts of the Tehran metropolitan. *Ghorbanian et al.* [2020] demonstrated the acceptable granular noise decrease to dissolve the difficulty relevant to the SAR data used for the broad application areas. A comparative analysis of filters is highlighted to figure out the performance of the filters and the ability to extract edges, lines, and points. *Dass and Yadav* [2020] Examined Radarset-2 images for the speckle containment with the Lee, Lee-sigma, Frost and Gamma-map. In common, the median & mean filters are also contained *Alves et al.* [2020], *Liu et al.* [2019], all filters are evaluated and show that some filters perform well in reducing the effect of granular noise and conserving the details of the edge.

The study aims to compare different filters' performance on AlosPalsar satellite bands for noise reduction and feature extraction in urban environments, focusing on the northwest region of Urmia City, Iran. Specifically, the Lee, Gamma-Map, Frost, and Average filters will be compared using *K*-means classification to identify the filter that provides the closest results to surface phenomena. Additionally, the study seeks to investigate the impact of the HV band's polarization properties and sensitivity on urban feature evaluation and resolution. Moreover, the research aims to determine the suitability of the SSI index for estimating noise-free gray levels. Overall, the study aims to contribute to improving remote sensing automation and monitoring of earth changes in sensitive areas such as natural resources, the environment, and agriculture.

The innovation of this paper lies in its application and evaluation of different spatial filters, specifically Lee, Frost, and Average filters, for monitoring urban complications using active remote sensing technologies. The paper focuses on comparing the effectiveness of these filters in identifying and characterizing urban features in the west of Urmia City using Landsat 8 satellite images and radar images with HH/HV polarization.

## 2. Study Area

Urmia locates in the central part of the province of West Azerbaijan, covering an area of about 5227 km<sup>2</sup> (Figure 1). It is the most populous city in the province, with a relative share of 31.28%. The study area shares borders with Turkey in the west, Lake Urmia in the east, the cities of Naqadeh, Mahabad, and Oshnavieh in the south, and Salmas in the north. According to the 2016 census, it has 736,224 inhabitants [*Fazel et al.*, 2017]. According to environmental considerations, the Urmia Basin's cities are vital in agricultural and industrial activities. There are 43 urban centers and 520 villages with about 7.3 million canteens, 9 to 10% of the total population. [*Fazel et al.*, 2017; *Nouri et al.*, 2017; *Shokati and Feizizadeh*, 2018].

## 3. Data and Methodology

### 3.1. Data

AlosPalsar radar images (HH and HV) sensors for the research area are used with a rare angle of 34.3 degrees. The second data used in this study is Landsat 8 bands (Blue, Near infrared, and Mid-infrared bands) for 2020 west Urmia City. Specifications of AlosPalsar Landsat 8 images are presented in Tables 1 and 2.

### 3.2. Geometric Correction and Calibration

In order to apply the geometric corrections for the radar images of the west Urmia City, the Snap 5.3 software was used. Then its pixel size was changed to 30 meters and the color image (HH-HV-HH/HV) RGB After generating the comment, the polarimetric images (HV) and (HH) are subject to geometric correction. The results showed that spectral

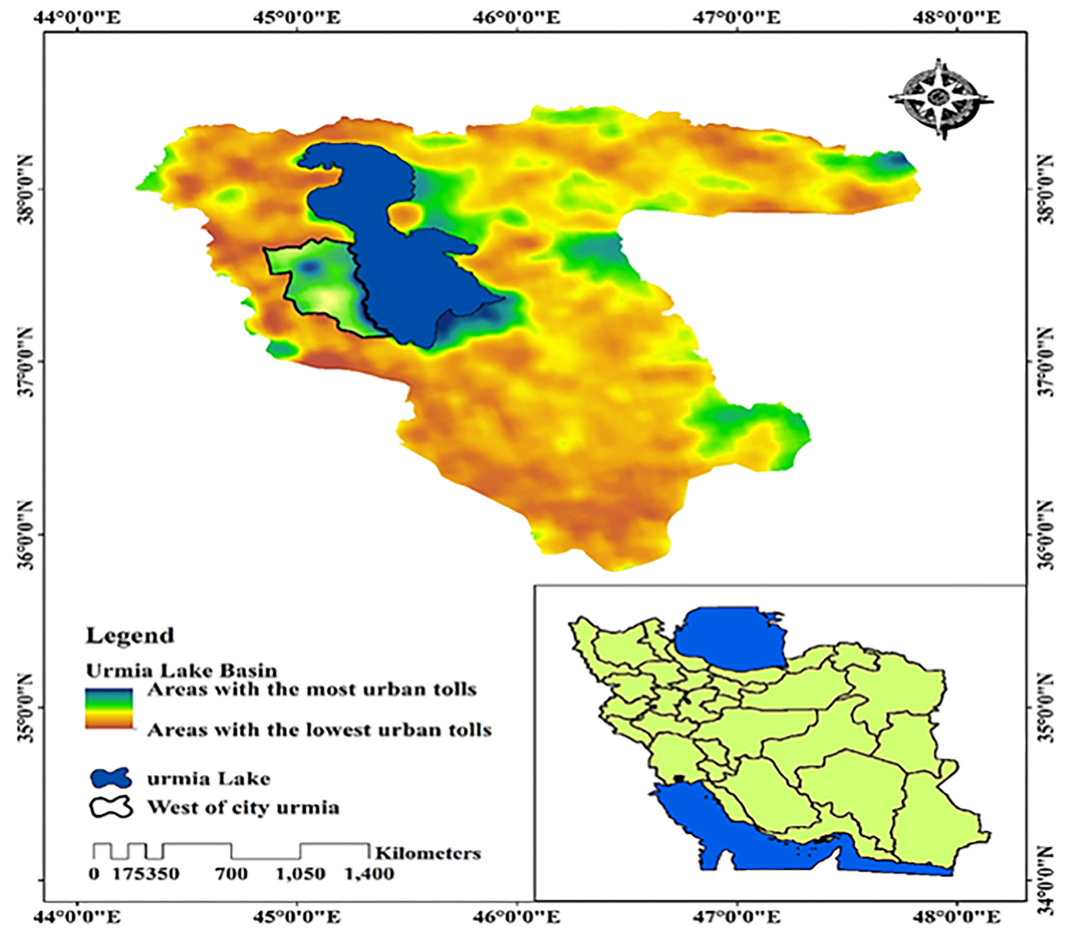


Figure 1. Study area west Urmia City.

Table 1. Profile of AlosPalsar radar images ([https://www.eorc.jaxa.jp/ALOS/en/alos/sensor/palsar\\_e.htm](https://www.eorc.jaxa.jp/ALOS/en/alos/sensor/palsar_e.htm))

Mode	Fine		ScanSAR	Polarimetric (Experimental mode)
Center Frequency	1270 MHz (L-band)			
Chirp Bandwidth	28 MHz	14 MHz	14 MHz, 28 MHz	14 MHz
Polarization	HH or VV	HH+HV or VV+VH	HH or VV	HH+HV+VH+VV
Incident angle	8 to 60°	8 to 60°	18 to 43°	8 to 30°
Range Resolution	7 to 44 m	14 to 88 m	100 m (multi look)	24 to 89 m
Observation Swath	40 to 70 km	40 to 70 km	250 to 350 km	20 to 65 km
Bit Length	5 bits	5 bits	5 bits	3 or 5 bits
Data rate	240 Mbps	240 Mbps	120 Mbps, 240 Mbps	240 Mbps
NE sigma zero	< -23 dB (Swath Width 70 km) < -25 dB (Swath Width 60 km)		< -25 dB	< -29 dB
S/A	> 16 dB (Swath Width 70 km) > 21 dB (Swath Width 60 km)		> 21 dB	> 19 dB
Radiometric accuracy	scene: 1 dB / orbit: 1.5 dB			

noise was observed in both produced images. The replay values of the HH/HV sensor polarizations are presented in Table 3. Methodology for identifying urban landscapes using radar and land images (Figure 2).

**Table 2.** Landsat satellite bands 8 OLI sensors (<http://mehdigis.blogfa.com/post/266>)

Spectral Bands	Wavelength in $\mu\text{m}$	Resolution in m
Coastal / Aerosol	0.433–0.453	30
Blue	0.450–0.515	30
Green	0.525–0.600	30
Red	0.630–0.680	30
Near Infrared	0.845–0.885	30
Short Wavelength Infrared	1.560–1.660	30
Short Wavelength Infrared	2.100–2.300	30
Panchromatic	0.500–0.680	15
Cirrus	1.360–1.390	30

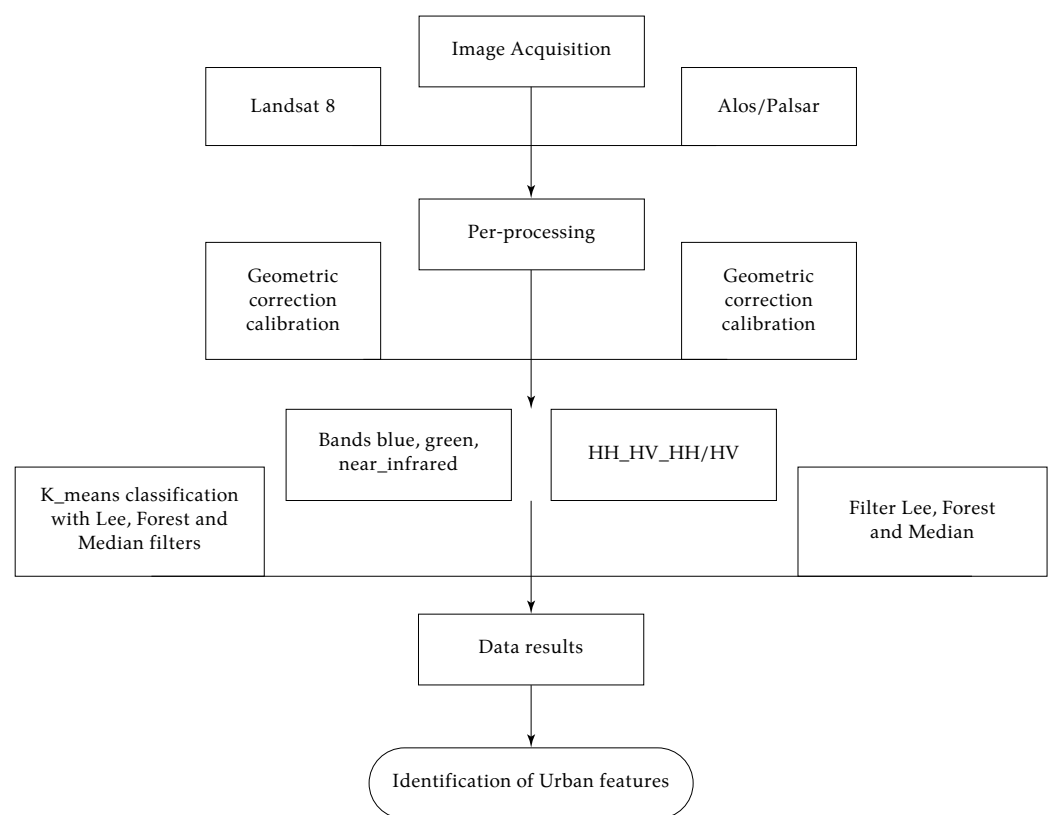


**Figure 2.** Workflow of the methodology.

**Table 3.** Sensor polarization replay values

Polarized	Min	Max	Mean	StdDev
HH	0.0005	22.5697	0.0987	0.4116
HV	0.0002	21.2345	0.0325	0.0721

#### 4. Results and Discussion

In order to improve the range of radar images and to distribute them in a better range, they were converted to decibels after calibration. The results showed that by applying this algorithm on each band, the output images of west Urmia City, had better brightness, and the phenomena that were not clear became somewhat more transparent. Calibrated imagery by the HH and HV bands is displayed in Figures 3 and 4.

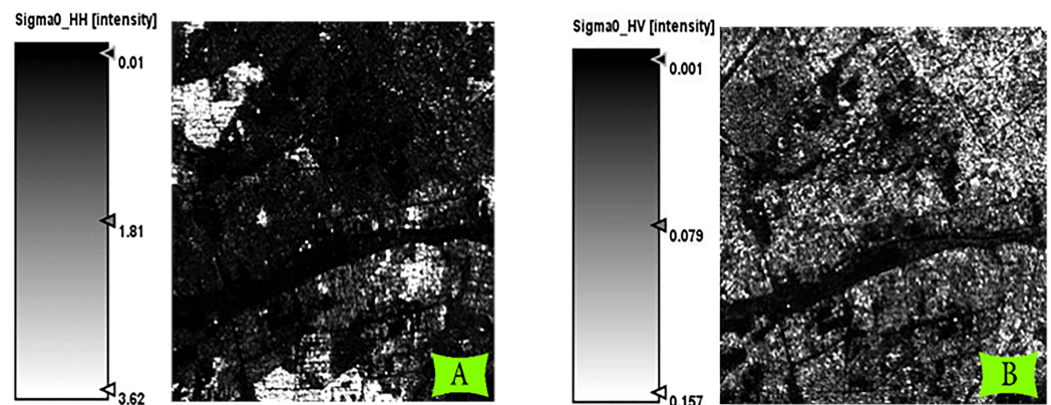


Figure 3. (a), HH and (b), for the HV band (calibrated) west of Urmia City.

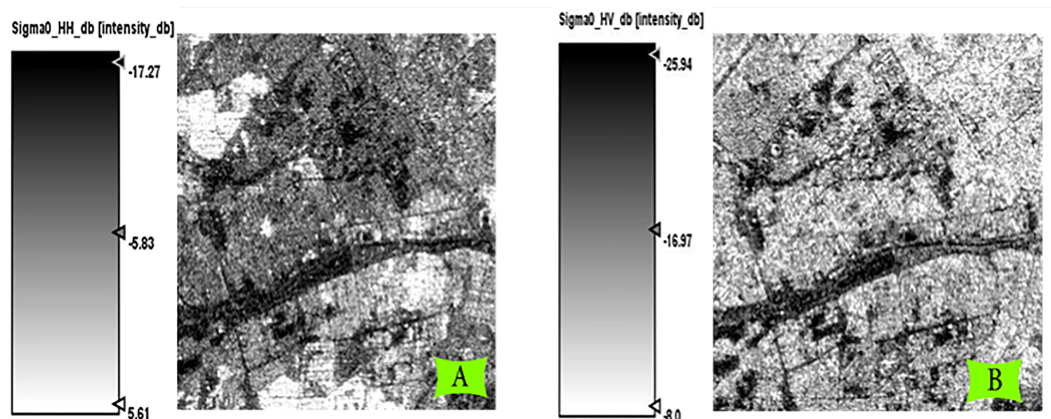


Figure 4. (a), calibrated HH band and, Sigma\_0 (b), calibrated HV band Sigma 0 and db west of Urmia City.

Figure 3, shows A of the HH band, with intensities ranging from (0.01 to 3.62%), and Figure B of the HV band, which has intensities ranging from (0.001 to 0.157%), which are brighter than the HH band. The donor is that image B of the HV band evaluates and identifies urban landscapes with greater accuracy.

While Figure 4a shows the calibrated HH band Sigma 0 converted to decibels, its values range from – (17.27% to 5.61%), and Figure 4b shows the calibrated HH band Sigma 0 converted to decibels. Bell is converted, and its values are between (–25.94% and –8.0%).

Therefore, it is assumed that after converting to Sigma0 and converting it to decibels, its intensity values are distributed and stretched in such a manner that it causes better and more precise detection of urban west of Urmia City features in the image. Additionally, it makes it possible to detect urban features. It Improves the image using the relevant histograms shown in Figure 5, where the distribution and elongation of the values can be observed.

#### 4.1. Average Filter

The Average filter is a regular averaging, which changes the central pixel’s value with the average of the surrounding pixel’s values. This filter has an excellent ability to smooth out noise. However, treating the moderation action the same will result in a reduction in resolution around sharp edges. Kernel windows with sizes of  $3 \times 3$  or  $5 \times 5$  are typically used to reduce this problem [Shanthy and Valarmathi, 2013].

Figure 6, presents the application of the average filter on the HH band with the kernel size  $3 \times 3 \times 5 \times 9 \times 9$ . Larger sizes are mixed, reducing the accuracy of the segregation of urban toll assessments. In addition to reducing spectral noise, selecting a  $3 \times 3$  kernel size

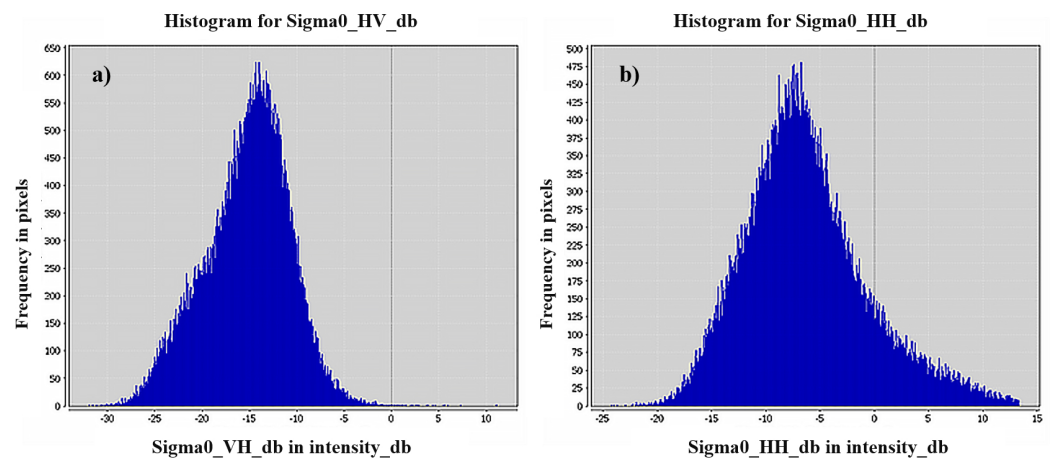


Figure 5. (a) sigma 0 calibrated HH band histogram converted to decibels, (b) and Sigma 0 calibrated HV band histogram converted to decibels.

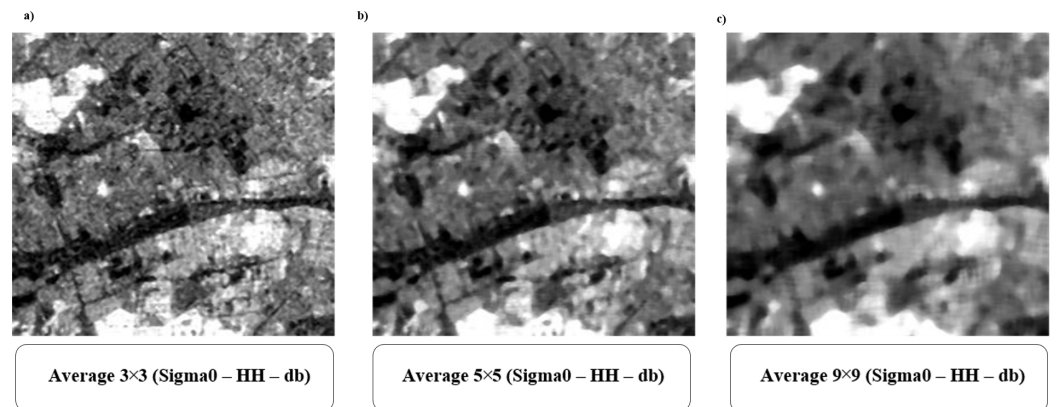


Figure 6. Average filter with kernel size (a) 3 × 3, (b) 5 × 5, (c) 9 × 9, applied on HH band (Sigma 0 – db) west of Urmia City.

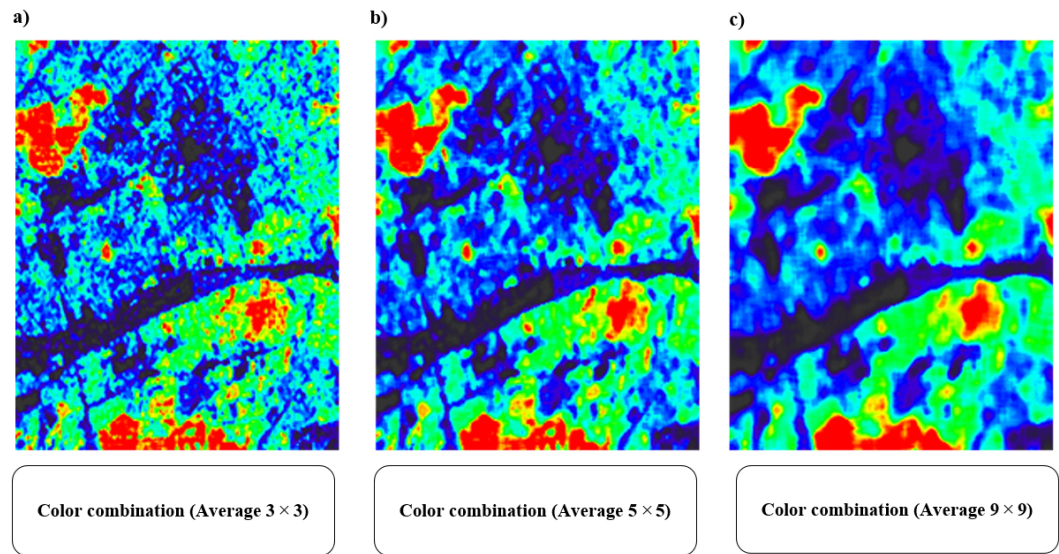
also displays the existing urban west of Urmia city features in the image in smaller pixel sizes. It makes the resolution of the features more accurate.

Figure 7, which, with expanding the kernel size of histogram values, has increased from (0 to 12.5%), which causes the smoothing of urban west of Urmia city features in the image Figure 8.

In previous studies, Urban features show themselves more accurately with minor changes in the values within the specified location. Alenin and Tyo [2014] examined a different despeckling algorithm for (SAR) data based on the shrinkage of the wavelet and non-local concepts. LaCasse et al. [2011] conducted research that combined two methods for constructing images based on mathematical structure. They proved that the demosaicking method corresponds with the channel filtering technique. However, when utilizing the implied filters in that technique, the constructed image with available objects in a higher part of frequencies resulted in a higher-quality image.

#### 4.2. Lee Filter

Jong-Sen-Lee established the Lee filter in 1982; the base concepts of these filters are Gaussian dispersion. In general, the statistical distribution of the image is the output of these filters. We acquire some statistical information such as median, Mean and Standard Deviation. This information provides the knowledge to assess the performance of speckle noise. The kernel size is also essential in speckle noise reduction and varies from 5 × 5 to 17 × 17 in some software such as snap. The size of kernels is odd numbers [Lee, 1986].



**Figure 7.** Color combination of average filter with kernel size (a)  $3 \times 3$ , (b)  $5 \times 5$ , (c)  $9 \times 9$ , applied on HH band (Sigma 0 – db) west of Urmia City.

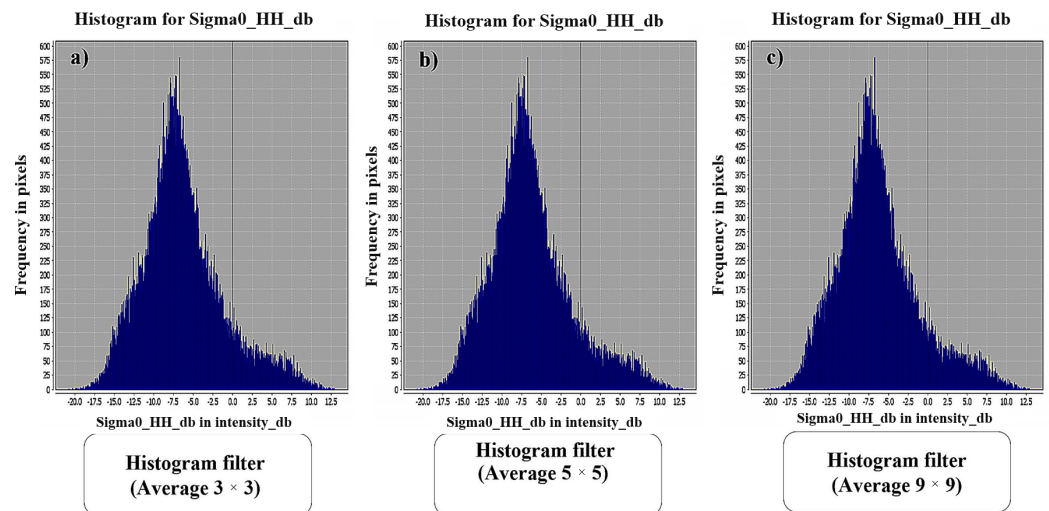


**Figure 8.** Mean histogram filter with kernel size (a)  $3 \times 3$ , (b)  $5 \times 5$ , (c)  $9 \times 9$ , applied on HH band (Sigma 0 – db).

Figure 9, presents the application of the Lee filter on the HH band with a kernel size  $3 \times 3 \times 5 \times 9 \times 9$ .

The image in the pixel is mixed in larger sizes, which reduces the resolution of the features with low density.

However, almost all three selected kernel sizes can accurately distinguish high-density urban west of Urmia City features. In the image, it should be displayed in smaller pixel sizes, and the resolution of the effects should be made with better accuracy. In Figure 10, the color combination of the Lee filter applied on the HH band with the kernel size  $3 \times 3$ ,  $5 \times 5$ ,  $9 \times 9$  confirms this result. However, the results obtained from Lee filter histograms on the HH band with kernel size  $3 \times 3$ ,  $5 \times 5$ ,  $9 \times 9$  show Figure 11 that with increasing kernel size, the histogram values from 0 to 12.5, also decrease to some extent. Finds that make the image Smooth.

Therefore, it could be mentioned that the more changes in the values in the mentioned range, the better the effects. In addition to the mentioned range of kernel size values  $3 \times 3$  and  $5 \times 5$ , other values are available that have unique functions in differentiating the effects. However, these values range between from  $-17.5$  to  $10$ . The kernel size histogram  $9 \times 9$  has

values ranging from  $-15.0$  to  $10$ . Expanding the kernel size results in a smoother image but reduces the accuracy of detecting complications with low density.

Lee *et al.* [2015] used the boxcar and sigma filters as initial filters. Nevertheless, extending the intended approach to most available filtering methods is uncomplicated. Moreover, the spatial filters vary commonly in the way of determining the adjacent uniform pixels [Lee *et al.*, 1999], the scattering model-based method [Lee *et al.*, 2006], the sigma range [Lee *et al.*, 2015], the scattering mechanism, and the intensity information [Wang *et al.*, 2016], homogeneity measurement [Lang *et al.*, 2015], NL [Chen *et al.*, 2011; Lang *et al.*, 2014], region growing [Vasile *et al.*, 2006].

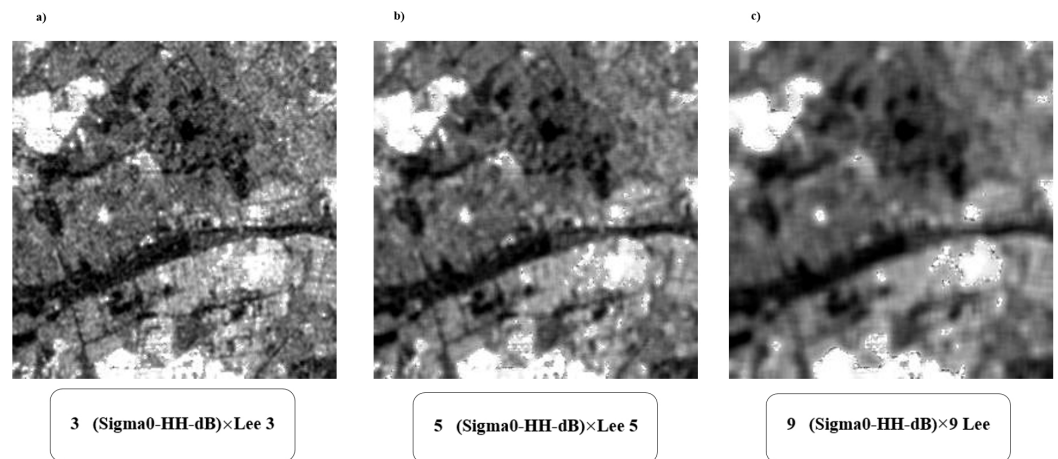


Figure 9. Lee filter with kernel size (a)  $3 \times 3$ , (b)  $5 \times 5$ , (c)  $9 \times 9$ , applied on the HH band (Sigma 0 – db) west of Urmia City.

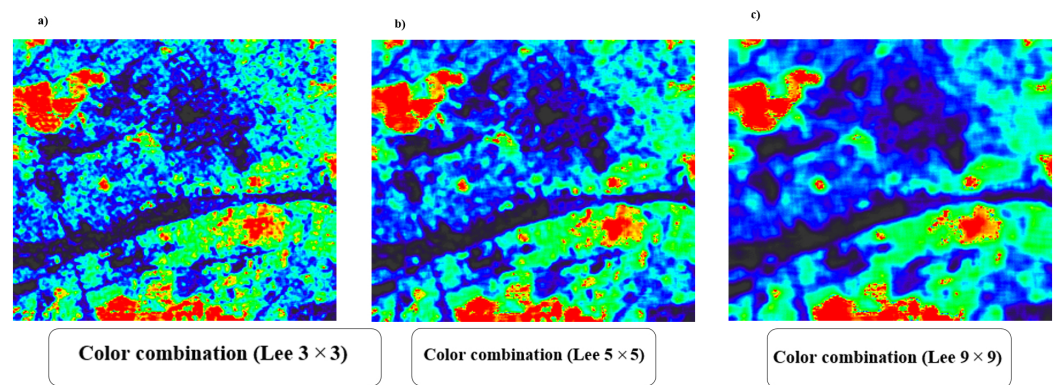
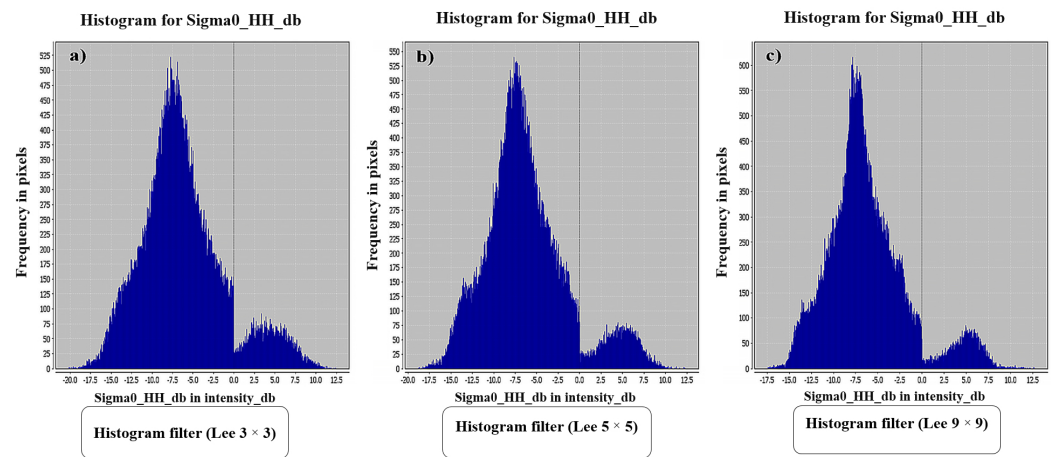


Figure 10. Combined Lee color filter with kernel size (a)  $3 \times 3$ , (b)  $5 \times 5$ , (c)  $9 \times 9$ , applied on HH band (Sigma 0 – db) west of Urmia City.

### 4.3. Frost Filter

The Frost filter is a widely used filter with variable parameters. It uses a weighted average on kernel pixels to soften images. The weight assigned to each pixel is a function of the kernel adjustment coefficient, mean, variance, and center pixel distance from the mean in the kernel gray [Frost *et al.*, 1982].

Figure 12, indicates the application of the Frost filter on the HH band with a kernel size  $3 \times 3 \times 5 \times 9 \times 9$ ; this increases the separation accuracy of high-density features. Nevertheless, almost all three selected kernel sizes can accurately distinguish high-density features. However, it is impossible to separate low-density tolls, and it causes urban tolls to be mixed. In addition to reducing separation accuracy, it also causes classification errors. In this filter, as in the previous filter, selecting a  $3 \times 3$  kernel size causes the effects in the image to be displayed in smaller pixel sizes and the resolution of the effects to be done more accurately,



**Figure 11.** Lee filter histogram with kernel size (a)  $3 \times 3$ , (b)  $5 \times 5$ , (c)  $9 \times 9$ , applied on HH band (Sigma0 – db).

in addition to reducing spectral noise. In [Figure 13](#), the color combination of the Frost filter applied on the HH band with the kernel size  $3 \times 3$ ,  $5 \times 5$ ,  $9 \times 9$  confirms this result.

However, the results obtained from the Frost filter histograms on the HH band with The kernel size  $3 \times 3$ ,  $5 \times 5$ ,  $9 \times 9$  show [Figure 14](#) with increasing the kernel size, the histogram values decrease from 0 to 12.), to some extent, which makes the image smoother. Therefore, it can be concluded that more changes in the values in the mentioned range show better effects on extracting urban west of Urmia City features. Also, kernel size values  $3 \times 3$  and  $5 \times 5$ , other than the mentioned range, differ, with values between 17.5.

They have ten and have their unique functions in differentiating different effects. According to the kernel size histogram  $9 \times 9$ , the values of which range from  $-15.0$  to  $10$ , the distribution of values of the histogram in this image becomes more compact. However, this indicates a more compact distribution of values in the histogram. It is worth mentioning that expanding the kernel size makes the image smoother and reduces the accuracy of detecting features with low density, making the distribution of intensity values more compact.

In previous studies, Improved AGGD-based noise reduction is presented to enhance the quality of the reconstructed image. Moreover, for quality enhancement, the cost of implementation is lower than the alternative methods (improved AGGD [[Golilarz et al., 2019](#)], HHO [[Golilarz et al., 2019](#)], and Bayes [[Chang et al., 2000](#)]).

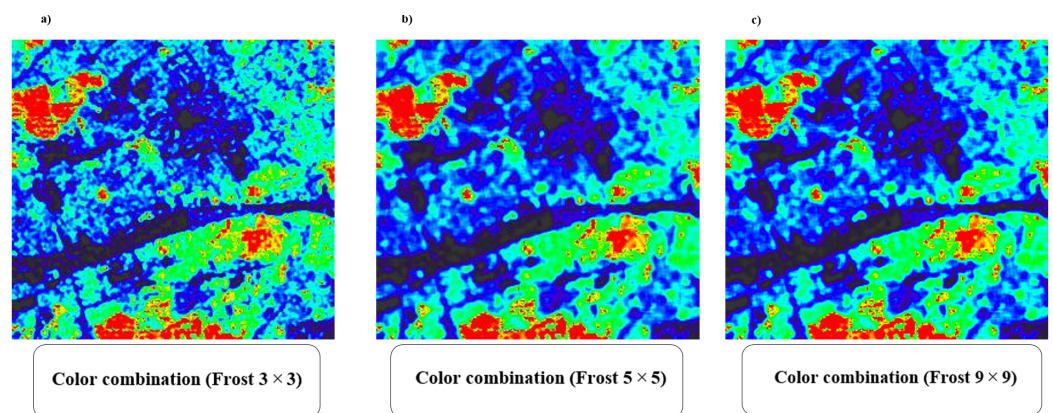


**Figure 12.** Frost filter with kernel size (a)  $3 \times 3$ , (b)  $5 \times 5$ , (c)  $9 \times 9$ , applied on HH band (Sigma 0 – db) west of Urmia City.

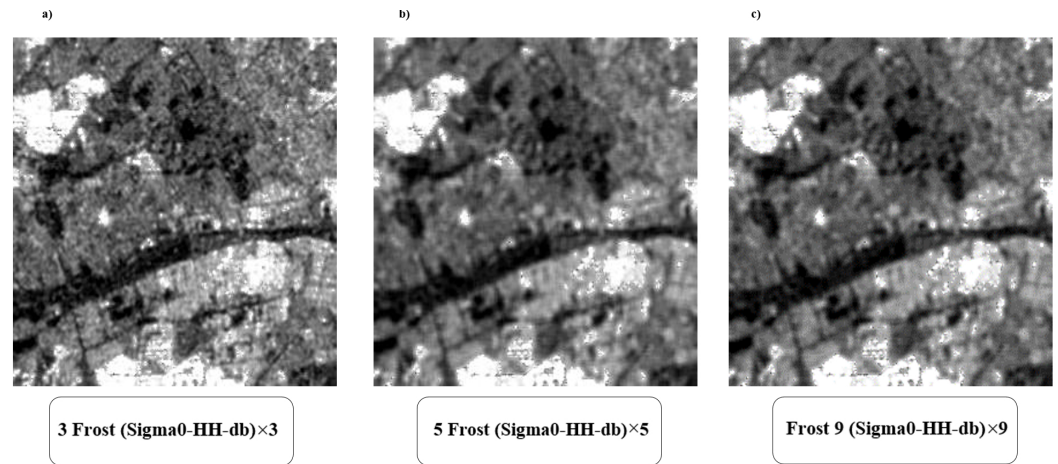


**Figure 13.** (a) frost filter with kernel size  $3 \times 3$ , (b)  $5 \times 5$ , (c)  $9 \times 9$  applied on HH band (Sigma 0 – db) west of Urmia City.

#### 4.4. Quantitative SSI Parameter

The quantitative SSI parameter in radar images is used to evaluate the filtering performance. The SSI parameter is a standard for quantifying and evaluating the performance of radar filters in which the average values of playback and standard deviation of images before and after application are used. Values less than one of these criteria indicate that the filter performed better. The SSI quantitative parameter was used to evaluate the performance of LEE, Average, and Frost filters, the results of which are presented in Table 4.

**Table 4.** SSI index values in different filter dimensions Average, Lee, Forst

SSI Parameter	Filters
0.563	Lee $3 \times 3$
0.675	Lee $5 \times 5$
0.896	Lee $7 \times 7$
0.590	Frost $3 \times 3$
0.601	Frost $5 \times 5$
0.789	Frost $9 \times 9$
0.683	Average $3 \times 3$
0.630	Average $5 \times 5$
0.785	Average $9 \times 9$

#### 4.5. Classification of Images by K-Means Method

According to Figure 14, four classes were extracted from the classification of K-means on Frost, Lee and Average filters. Comparing filters with the classification results on Landsat 8 images showed that the closest result is accurate. Above is the Lee filter with a  $3 \times 3$  size kernel. The total accuracy obtained is (97.36%), and the kappa coefficient is (0.96%). Between a classified land cover map and a reference or actual land map, the producer error is related to the percentage of pixels related to the classes but classified as other classes. On the other hand, user error is an error that is calculated based on user accuracy and is equivalent to the percentage of pixels that do not belong to the class in question but are considered in that classification.

#### 5. Conclusion

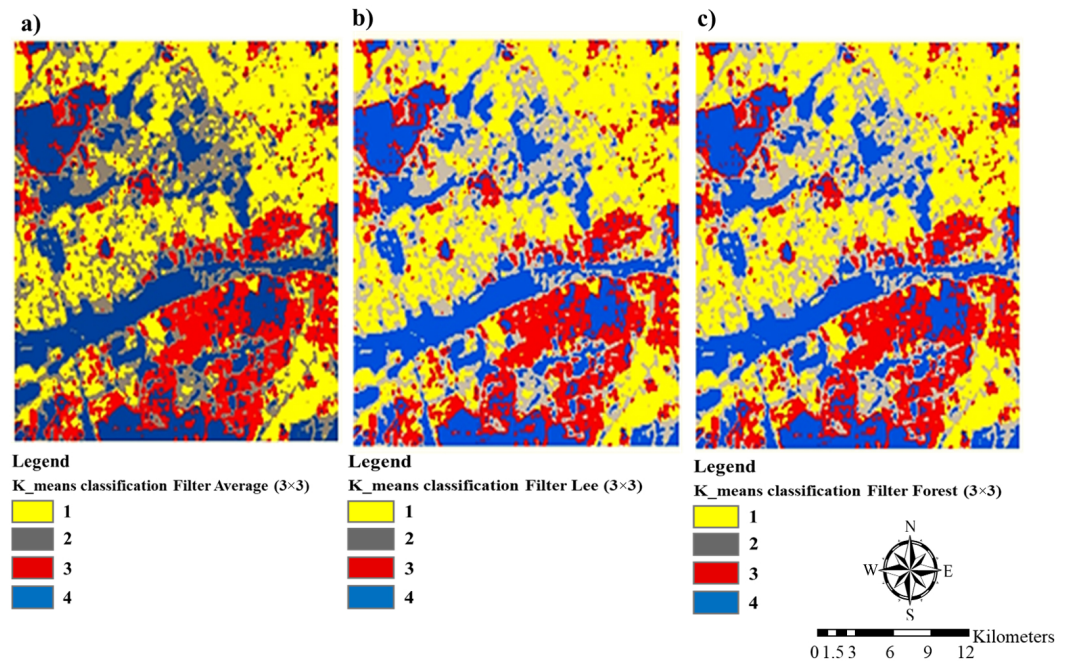


**Figure 14.** Classification of (a) *K*-means Average filter, (b) Lee filter, (c) Frost filter west of Urmia City.

Nowadays, images with the appropriate spatial and spectral resolution are often used to monitor the earth for various purposes, such as detecting changes, classifying land cover, and diagnosing complications. These techniques are especially important when data is used in sensitive areas such as the environment, natural resources, and agriculture. Based on the outputs obtained in this study, it has been shown that the HV band has better evaluation and resolution in an urban environment with artificial features such as buildings and different metal structures due to its polarization properties and sensitivity to the phenomenon in the city. In this study, different filters were applied on the images of both AlosPalsar satellite bands to estimate the degree of noise-free gray in the northwest of Urmia City according to the averages through the SSI index. The results include filters that can help reduce spike noise in AlosPalsar satellite radar images, such as the Lee filter with  $3 \times 3$  kernel size.

Additionally, it is essential to note that the output from the filters may vary depending on the bands of the AlosPalsar satellite. However, after conducting *K*-means classification on Lee, Gamma-Map, Frost, and Average filters, the Lee filter with a  $3 \times 3$  kernel size has been identified to provide the closest results to surface phenomena. Specifically, it produced a kappa coefficient of 0.96% and an accuracy of 97.36% in the northwest area of Urmia. Future research could include exploring the impact of different filter parameters on noise reduction and feature extraction accuracy in urban environments and comparing the results of different satellite systems in monitoring earth changes in sensitive areas.

**Acknowledgments.** We, the authors, thank the respected reviewers for reviewing this article. The research does not receive any funding. Data will be available based on request.

## References

- Abdollahi, A., H. R. R. Bakhtiari, and M. P. Nejad (2017), Investigation of SVM and Level Set Interactive Methods for Road Extraction from Google Earth Images, *Journal of the Indian Society of Remote Sensing*, 46(3), 423–430, <https://doi.org/10.1007/s12524-017-0702-x>.
- Alenin, A. S., and J. S. Tyo (2014), Generalized channeled polarimetry, *Journal of the Optical Society of America A*, 31(5), 1013, <https://doi.org/10.1364/josaa.31.001013>.

- Alves, W. A. L., C. F. Gobber, D. J. Silva, A. Morimitsu, R. F. Hashimoto, and B. Marcotegui (2020), Image segmentation based on ultimate levelings: From attribute filters to machine learning strategies, *Pattern Recognition Letters*, 133, 264–271, <https://doi.org/10.1016/j.patrec.2020.03.013>.
- Attarchi, S., M. Poorrahimi, and V. Isazade (2020), Comparison of spectral indices and object-based classification for built-up area extraction in different urban areas, *Geographical Urban Planning Research (GUPR)*, 8(1), 23–43, <https://doi.org/10.22059/jurbangeo.2020.299492.1249>.
- Betbeder, J., S. Rapinel, S. Corgne, E. Pottier, and L. Hubert-Moy (2015), TerraSAR-X dual-pol time-series for mapping of wetland vegetation, *ISPRS Journal of Photogrammetry and Remote Sensing*, 107, 90–98, <https://doi.org/10.1016/j.isprsjprs.2015.05.001>.
- Camargo, F. F., E. E. Sano, C. M. Almeida, J. C. Mura, and T. Almeida (2019), A Comparative Assessment of Machine-Learning Techniques for Land Use and Land Cover Classification of the Brazilian Tropical Savanna Using ALOS-2/PALSAR-2 Polarimetric Images, *Remote Sensing*, 11(13), 1600, <https://doi.org/10.3390/rs11131600>.
- Chang, S. G., B. Yu, and M. Vetterli (2000), Adaptive wavelet thresholding for image denoising and compression, *IEEE Transactions on Image Processing*, 9(9), 1532–1546, <https://doi.org/10.1109/83.862633>.
- Chen, J., Y. Chen, W. An, Y. Cui, and J. Yang (2011), Nonlocal Filtering for Polarimetric SAR Data: A Pretest Approach, *IEEE Transactions on Geoscience and Remote Sensing*, 49(5), 1744–1754, <https://doi.org/10.1109/tgrs.2010.2087763>.
- Dai, J., T. Zhu, Y. Wang, R. Ma, and X. Fang (2020), Road Extraction From High-Resolution Satellite Images Based on Multiple Descriptors, *IEEE Journal of Selected Topics in Applied Earth Observations and Remote Sensing*, 13, 227–240, <https://doi.org/10.1109/jstars.2019.2955277>.
- Dass, R., and N. Yadav (2020), Image Quality Assessment Parameters for Despeckling Filters, *Procedia Computer Science*, 167, 2382–2392, <https://doi.org/10.1016/j.procs.2020.03.291>.
- Fazel, N., R. Berndtsson, C. B. Uvo, K. Madani, and B. Kløve (2017), Regionalization of precipitation characteristics in Iran's Lake Urmia basin, *Theoretical and Applied Climatology*, 132(1-2), 363–373, <https://doi.org/10.1007/s00704-017-2090-0>.
- Frost, V. S., J. A. Stiles, K. S. Shanmugan, and J. C. Holtzman (1982), A Model for Radar Images and Its Application to Adaptive Digital Filtering of Multiplicative Noise, *IEEE Transactions on Pattern Analysis and Machine Intelligence*, PAMI-4(2), 157–166, <https://doi.org/10.1109/tpami.1982.4767223>.
- Ghanbari, A., V. Isazade, and Z. Alibeigy (2022), Analysis of Spatial Justice in Dealing with Urban Facilities Using Quantitative, Spatial and Moran Correlation Models (Study Area: Isfahan), *Journal Research and Urban Planning*, 13(50), 240–254.
- Ghorbanian, A., M. Kakooei, M. Amani, S. Mahdavi, A. Mohammadzadeh, and M. Hasanlou (2020), Improved land cover map of Iran using Sentinel imagery within Google Earth Engine and a novel automatic workflow for land cover classification using migrated training samples, *ISPRS Journal of Photogrammetry and Remote Sensing*, 167, 276–288, <https://doi.org/10.1016/j.isprsjprs.2020.07.013>.
- Golilarz, N. A., H. Gao, and H. Demirel (2019), Satellite Image De-Noising With Harris Hawks Meta Heuristic Optimization Algorithm and Improved Adaptive Generalized Gaussian Distribution Threshold Function, *IEEE Access*, 7, 57,459–57,468, <https://doi.org/10.1109/access.2019.2914101>.
- Hu, T., J. Yang, X. Li, and P. Gong (2016), Mapping Urban Land Use by Using Landsat Images and Open Social Data, *Remote Sensing*, 8(2), 151, <https://doi.org/10.3390/rs8020151>.
- Isazade, V., A. Ghanbari, and K. Valizadeh (2021), Evaluation of spectral indices and extraction of constructed and non-constructed urban features and its comparison with ground surface temperature using Landsat 7 and 8 satellite images (Study area, Tehran), *Journal of Spatial Planning*, 11(4), 23–39, <https://doi.org/10.30488/GPS.2021.243118.3283>.
- Isazade, V., A. B. Qasimi, and E. Isazade (2022), Environmental dust effect phenomenon on the sustainability of urban areas using remote sensing data in GEE, *Safety in Extreme Environments*, 5(1), 59–67, <https://doi.org/10.1007/s42797-022-00067-z>.

- Kaushik, K., and D. Kumar (2020), Forest Disturbance Mapping with Microwave Remote Sensing, *Journal of Landscape Ecology*, 13(2), 95–128, <https://doi.org/10.2478/jlecol-2020-0012>.
- Kraus, K. (2003), Photogrammetry, Remote Sensing and Spatial Information Sciences for heritage documentation, in *Proceedings of the XIXth International Symposium, CIPA 2003: new perspectives to save cultural heritage*, pp. 17–24, CIPA 2003 Organising Committee, Antalya (Turkey).
- LaCasse, C. F., R. A. Chipman, and J. S. Tyo (2011), Band limited data reconstruction in modulated polarimeters, *Optics Express*, 19(16), 14,976, <https://doi.org/10.1364/oe.19.014976>.
- Lang, F., J. Yang, D. Li, L. Shi, and J. Wei (2014), Mean-Shift-Based Speckle Filtering of Polarimetric SAR Data, *IEEE Transactions on Geoscience and Remote Sensing*, 52(7), 4440–4454, <https://doi.org/10.1109/tgrs.2013.2282036>.
- Lang, F., J. Yang, and D. Li (2015), Adaptive-Window Polarimetric SAR Image Speckle Filtering Based on a Homogeneity Measurement, *IEEE Transactions on Geoscience and Remote Sensing*, 53(10), 5435–5446, <https://doi.org/10.1109/tgrs.2015.2422737>.
- Lapini, A., S. Pettinato, E. Santi, S. Paloscia, G. Fontanelli, and A. Garzelli (2020), Comparison of Machine Learning Methods Applied to SAR Images for Forest Classification in Mediterranean Areas, *Remote Sensing*, 12(3), 369, <https://doi.org/10.3390/rs12030369>.
- Lee, J.-S. (1986), Speckle Suppression And Analysis For Synthetic Aperture Radar Images, *Optical Engineering*, 25(5), 255,636, <https://doi.org/10.1117/12.7973877>.
- Lee, J.-S., M. R. Grunes, and G. de Grandi (1999), Polarimetric SAR speckle filtering and its implication for classification, *IEEE Transactions on Geoscience and Remote Sensing*, 37(5), 2363–2373, <https://doi.org/10.1109/36.789635>.
- Lee, J.-S., M. R. Grunes, D. L. Schuler, E. Pottier, and L. Ferro-Famil (2006), Scattering-model-based speckle filtering of polarimetric SAR data, *IEEE Transactions on Geoscience and Remote Sensing*, 44(1), 176–187, <https://doi.org/10.1109/tgrs.2005.859338>.
- Lee, J.-S., T. L. Ainsworth, Y. Wang, and K.-S. Chen (2015), Polarimetric SAR Speckle Filtering and the Extended Sigma Filter, *IEEE Transactions on Geoscience and Remote Sensing*, 53(3), 1150–1160, <https://doi.org/10.1109/tgrs.2014.2335114>.
- Leiva-Murillo, J. M., L. Gomez-Chova, and G. Camps-Valls (2013), Multitask Remote Sensing Data Classification, *IEEE Transactions on Geoscience and Remote Sensing*, 51(1), 151–161, <https://doi.org/10.1109/TGRS.2012.2200043>.
- Li, Y., S. Wang, Q. Zhao, and G. Wang (2020), A new SAR image filter for preserving speckle statistical distribution, *Signal Processing*, 176, 107,706, <https://doi.org/10.1016/j.sigpro.2020.107706>.
- Liu, N., Z. Cao, Z. Cui, Y. Pi, and S. Dang (2019), Multi-Scale Proposal Generation for Ship Detection in SAR Images, *Remote Sensing*, 11(5), 526, <https://doi.org/10.3390/rs11050526>.
- Mohan, M., and A. Kandya (2015), Impact of urbanization and land-use/land-cover change on diurnal temperature range: A case study of tropical urban airshed of India using remote sensing data, *Science of The Total Environment*, 506-507, 453–465, <https://doi.org/10.1016/j.scitotenv.2014.11.006>.
- Mun, J., Y. Jang, Y. Nam, and J. Kim (2019), Edge-enhancing bi-histogram equalisation using guided image filter, *Journal of Visual Communication and Image Representation*, 58, 688–700, <https://doi.org/10.1016/j.jvcir.2018.12.037>.
- NISAR (2018), *NASA-ISRO SAR (NISAR) Mission Science Users' Handbook*, NASA Jet Propulsion Laboratory.
- Nouri, H., R. J. Mason, and N. Moradi (2017), Land suitability evaluation for changing spatial organization in Urmia County towards conservation of Urmia Lake, *Applied Geography*, 81, 1–12, <https://doi.org/10.1016/j.apgeog.2017.02.006>.
- Osgouei, P. E., S. Kaya, E. Sertel, and U. Alganci (2019), Separating Built-Up Areas from Bare Land in Mediterranean Cities Using Sentinel-2A Imagery, *Remote Sensing*, 11(3), 345, <https://doi.org/10.3390/rs11030345>.
- Podest, E. (2018), *SAR for Mapping Land Cover*, National Aeronautics and Space Administration.

- Qasimi, A. B., V. Isazade, G. Kaplan, and Z. Nadry (2022), Spatiotemporal and multi-sensor analysis of surface temperature, NDVI, and precipitation using google earth engine cloud computing platform, *Russian Journal of Earth Sciences*, 22(6), 1–12, <https://doi.org/10.2205/2022ES000812>.
- Rasche, C. (2018), Rapid contour detection for image classification, *IET Image Processing*, 12(4), 532–538, <https://doi.org/10.1049/iet-ipr.2017.1066>.
- Routray, S., P. P. Malla, S. K. Sharma, S. K. Panda, and G. Palai (2020), A new image denoising framework using bilateral filtering based non-subsampled shearlet transform, *Optik*, 216, 164,903, <https://doi.org/10.1016/j.ijleo.2020.164903>.
- Seo, S. (2018), Subpixel Edge Localization Based on Adaptive Weighting of Gradients, *IEEE Transactions on Image Processing*, 27(11), 5501–5513, <https://doi.org/10.1109/tip.2018.2860241>.
- Seo, S. (2019a), Subpixel Line Localization With Normalized Sums of Gradients and Location Linking With Straightness and Omni-Directionality, *IEEE Access*, 7, 155–167, <https://doi.org/10.1109/access.2019.2959320>.
- Seo, S. (2019b), Line-Detection Based on the Sum of Gradient Angle Differences, *Applied Sciences*, 10(1), 254, <https://doi.org/10.3390/app10010254>.
- Serwa, A. (2020), Studying the Potentiality of Using Digital Gaussian Pyramids in Multi-spectral Satellites Images Classification, *Journal of the Indian Society of Remote Sensing*, 48(12), 1651–1660, <https://doi.org/10.1007/s12524-020-01173-w>.
- Serwa, A., and S. Elbially (2021), Enhancement of classification accuracy of multi-spectral satellites' images using Laplacian pyramids, *The Egyptian Journal of Remote Sensing and Space Science*, 24(2), 283–291, <https://doi.org/10.1016/j.ejrs.2020.12.006>.
- Serwa, A., and M. Saleh (2021), New semi-automatic 3D registration method for terrestrial laser scanning data of bridge structures based on artificial neural networks, *The Egyptian Journal of Remote Sensing and Space Science*, 24(3, Part 2), 787–798, <https://doi.org/10.1016/j.ejrs.2021.06.003>.
- Seto, K. C., B. Güneralp, and L. R. Hutyrá (2012), Global forecasts of urban expansion to 2030 and direct impacts on biodiversity and carbon pools, *Proceedings of the National Academy of Sciences*, 109(40), 16,083–16,088, <https://doi.org/10.1073/pnas.1211658109>.
- Shanthi, I., and M. L. Valarmathi (2013), SAR image despeckling using possibilistic fuzzy C-means clustering and edge detection in bandelet domain, *Neural Computing and Applications*, 23(S1), 279–291, <https://doi.org/10.1007/s00521-013-1394-y>.
- Shi, Y., Q. Li, and X. X. Zhu (2019), Building Footprint Generation Using Improved Generative Adversarial Networks, *IEEE Geoscience and Remote Sensing Letters*, 16(4), 603–607, <https://doi.org/10.1109/LGRS.2018.2878486>.
- Shokati, B., and B. Feizizadeh (2018), Sensitivity and uncertainty analysis of agro-ecological modeling for saffron plant cultivation using GIS spatial decision-making methods, *Journal of Environmental Planning and Management*, 62(3), 517–533, <https://doi.org/10.1080/09640568.2018.1427561>.
- Sun, H., W. Forsythe, and N. Waters (2007), Modeling Urban Land Use Change and Urban Sprawl: Calgary, Alberta, Canada, *Networks and Spatial Economics*, 7(4), 353–376, <https://doi.org/10.1007/s11067-007-9030-y>.
- Vasile, G., E. Trouve, J.-S. Lee, and V. Buzuloiu (2006), Intensity-driven adaptive-neighborhood technique for polarimetric and interferometric SAR parameters estimation, *IEEE Transactions on Geoscience and Remote Sensing*, 44(6), 1609–1621, <https://doi.org/10.1109/tgrs.2005.864142>.
- Wang, Y., J. Yang, and J. Li (2016), Similarity-intensity joint PolSAR speckle filtering, in *2016 CIE International Conference on Radar (RADAR)*, pp. 1–5, <https://doi.org/10.1109/RADAR.2016.8059213>.
- Wei, C., and T. Blaschke (2018), Pixel-Wise vs. Object-Based Impervious Surface Analysis from Remote Sensing: Correlations with Land Surface Temperature and Population Density, *Urban Science*, 2(1), <https://doi.org/10.3390/urbansci2010002>.

- Yang, C. H., B. K. Kenduywo, and U. Soergel (2016), Change detection based on persistent scatterer interferometry – a new method of monitoring building changes, *ISPRS Annals of the Photogrammetry, Remote Sensing and Spatial Information Sciences*, III-7, 243–250, <https://doi.org/10.5194/isprs-annals-III-7-243-2016>.
- Zakeri, H., F. Yamazaki, and W. Liu (2017), Texture Analysis and Land Cover Classification of Tehran Using Polarimetric Synthetic Aperture Radar Imagery, *Applied Sciences*, 7(5), 452, <https://doi.org/10.3390/app7050452>.
- Zia, S., S. A. Shirazi, M. N. Bhalli, and S. Kausar (2015), The Impact Of Urbanization On Mean Annual Temperature Of Lahore Metropolitan Area, Pakistan, *Pakistan Journal of Science*, 67(3).